FULL PAPER

High-resolution 3D earthquake forecasting beneath the greater Tokyo area

Yosihiko Ogata[1*] , Koich Katsura[1], Hiroshi Tsuruoka[2] and Naoshi Hirata[2]

Abstract

We propose an extended 3D space (longitude, latitude, and depth) epidemic-type aftershock sequence (ETAS) model for seismicity forecasts beneath the greater Tokyo area (the Kanto region), which also takes into account the effects induced by the M9 Tohoku-Oki earthquake of 2011. The model is characterized by a number of 3D location-dependent parameters, such as the background seismicity rates, and the productivity rate induced by the Tohoku earthquake. These allow production of high-resolution predictive mappings in zones where hypocenters are densely populated. The optimally inverted 3D spatial images of the characterizing parameters effectively discriminate seismicity features in the crust and near the plate boundaries. The success of the model is demonstrated using short-, intermediate- and long-term probability forecasts of intermediate and large earthquake occurrences beneath the Kanto region.

Keywords: 3D Delaunay tessellation, Hierarchical space–time ETAS model, Induced seismicity, Penalized log likelihood function, Akaike's Bayesian Criterion, M9 Tohoku-Oki Earthquake

Introduction and data

The dense population of the Tokyo metropolis prompted the government's Earthquake Research Committee (2004) to predict, and subsequently update, the long-term probability of an M7 class earthquake beneath the southern Kanto Plain. The estimated occurrence probability of such an earthquake, during the next 30 years, is 70–80%. This estimate is based on earthquake records since 1885 (Utsu 1982), a number of historical disastrous earthquakes (e.g. Utsu 2002), assumption of a stationary temporal Poisson process, and application of the Gutenberg–Richter (GR) law in the focal area. However, there has been little prior study of the spatial distribution of event probabilities associated with such a forecast.

The Kanto region urgently requires a 3D short- and medium-term seismicity forecasting model. Because three tectonic plates meet beneath Kanto Plain (see Fig. 1), their interactions, and hence forecasting of the occurrence of inter-plate and intraplate earthquakes, are too complex for approaches such as the 2D space–time epidemic-type aftershock sequence (ETAS) models, as

proposed by Ogata (2011), which ignores the depths of earthquakes.
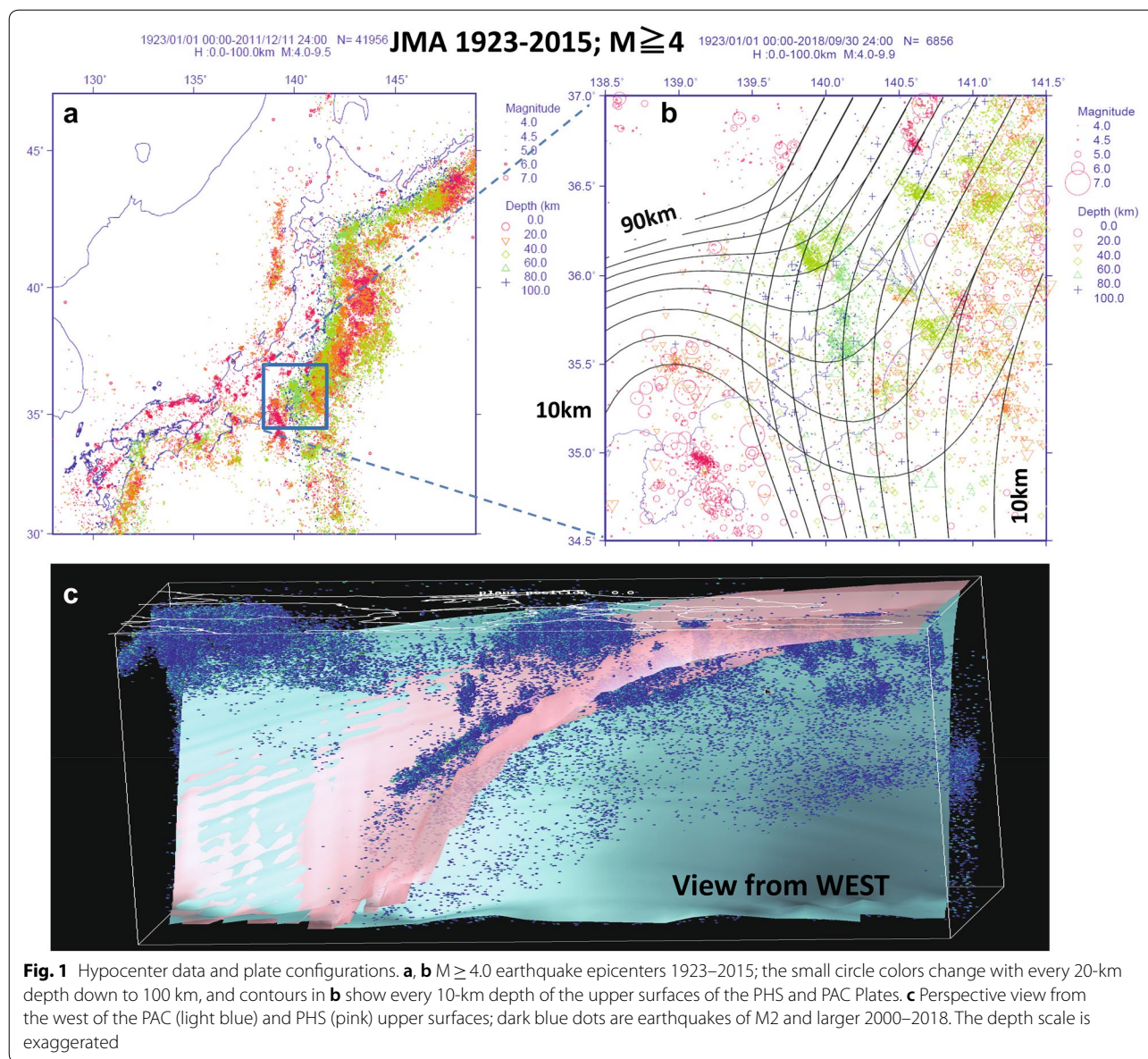
Recently, Guo et al. (2018) applied a 3D space–time ETAS model in the Kanto region. They separated depth effects from the horizontal 2D space, and showed that such a separable 3D model fits observations significantly better than the 2D model. However, it is known that earthquake occurrence rates are significantly dependent on the configuration of the interacting and colliding plates beneath the Kanto Plain. Hence, we here define a flexible 3D hierarchical space–time ETAS model that allows for such effects. Furthermore, recent seismic activity beneath the Kanto region has been induced by the M9 Tohoku-Oki earthquake of March 11, 2011. Indeed, Ishibe et al. (2011) reported increased seismicity rates in many subregions in the Kanto area. Thus, new modeling should take this induced effect into consideration (e.g., Dietrich 1994; Parsons et al. 2012).

Our focus was the Kanto cuboid bounded by 138.5°–141.5°E and 34.5°–37.0°N, down to a depth of 100 km, as shown in Fig. 1. We have used space–time locations and magnitudes of earthquakes of $M \geq 4$ selected from the Hypocenter Catalog of the Japan Meteorological Agency (JMA 2018) from 1923 to 2015. Our model-fitting target period was from 1926 to 2015, but we also considered

*Correspondence: ogata@ism.ac.jp
[1] The Institute of Statistical Mathematics, 10-3 Midori-Cho,Tachikawa, Tokyo 190-8562, Japan
Full list of author information is available at the end of the article

Ogata *et al. Earth, Planets and Space* (2019) 71:113

Page 2 of 14

Fig. 1 Hypocenter data and plate configurations. **a**, **b** M ≥ 4.0 earthquake epicenters 1923–2015; the small circle colors change with every 20-km depth down to 100 km, and contours in **b** show every 10-km depth of the upper surfaces of the PHS and PAC Plates. **c** Perspective view from the west of the PAC (light blue) and PHS (pink) upper surfaces; dark blue dots are earthquakes of M2 and larger 2000–2018. The depth scale is exaggerated

the precursory period from 1923 to 1925, including the M7.9 great Kanto earthquake of September 1, 1923. This ensured the stationarity of the ETAS models in the target period.

The hypocenters well delineate the plate boundaries (Fig. 1b, c), after the unification of catalogs post October 1997 (cf., Acknowledgements). In this work, we adopted the Philippine Sea (PHS) Plate and the Pacific (PAC) Plate models due to Hashimoto et al. (2004) and Hashimoto and Matsu'ura (2006). There have been many different depth models proposed for the PHS Plate configuration beneath the Kanto region, mainly based on the spatial distribution of the micro earthquakes since Kasahara

(1985). Also, recently, the plate boundaries in some zones have been partly delineated using repeating earthquakes (e.g., Kimura et al. 2006; Uchida et al. 2010). Our adopted plate models, covering the entire Kanto region, have been developed using cubic spline surfaces determined on the basis of tectonic loading mechanics and seismic, geodetic, geologic, and geomorphic data. They are also reasonably consistent with the recent boundaries based on repeating earthquakes.

In this manuscript, we first apply the temporal ETAS model to see the change of seismicity in the Kanto region, before and after the M9 Tohoku-Oki earthquake. Then, we analyze the seismic activity beneath the Kanto Plain

Ogata *et al. Earth, Planets and Space* (2019) 71:113

Page 3 of 14

using a 3D model taking the induced effects of the M9 Tohoku-Oki earthquake into consideration. The model characteristic parameters are location dependent and we estimate them using an empirical Bayesian method (Akaike 1980) to forecast the probabilities of occurrence beneath the Kanto plain. Also, we show the inverted 3D spatial images of such characteristic parameters illustrate the discriminative seismicity patterns in the crust and on the subducting plates boundaries.

Seismicity beneath Kanto Region

Temporal seismicity

The temporal epidemic-type aftershock sequence (ETAS) model (Ogata 1985, 1988, 1989) predicts occurrence rates based on the occurrence times and magnitudes of past earthquakes. However, Fig. 2a indicates a significant deviation after the 2011 M9 Tohoku-Oki earthquake. As the M9 earthquake occurred outside of our study region, we must add an Omori–Utsu type function (Utsu et al. 1995) in such a way that

$$\lambda_A^{ETAS+OU}(t|H_t) = \mu + \sum_{t_i < t, \ t_i \neq t_{M9}} \frac{K_0 e^{\alpha(M_i - M_c)}}{(t - t_i + c)^p}$$
$$+ \frac{K_{M9} \cdot H(t - t_{M9})}{(t - t_{M9} + c_{M9})^{p_{M9}}}, \quad (1)$$

where t_{M9} is the time of occurrence of the M9 Tohoku-Oki earthquake. Here, the Heaviside function, associated with the Omori–Utsu type function, is $H(s) = 1$ for $s > 0$, $H(s) = 0$ otherwise. The time decay coefficient could be $p_{M9} = 1.0$, according to the triggering effect discussed by Dietrich (1994), but we have adopted the maximum likelihood estimate (MLE), as described in Fig. 2b, which actually provides a better fit.

Figure 2b clearly shows that the model in Eq. (1) fits well throughout the entire period until 2015, and Fig. 2c shows how the expected cumulative model numbers, in the entire Kanto region, were decomposed into those of the three components; background rates, self-triggering rates (aftershock productivity), and the intensity factor induced by the M9 event. We found that the self-exciting trigger effect and the induced effect of the external M9 event are of roughly similar size.

Hierarchical 3D ETAS Model with externally induced effect

Suppose that we have observed earthquakes at time–space–magnitude coordinates $H_t = \{(t_n, x_n, y_n, z_n), M_n \geq M_c; \ n = 1, 2, \ldots, N\}$ over a period $[S, t]$ until time t and in the cuboid down to 100-km depth beneath the Kanto region. Here, we propose a 3D hierarchical space–time epidemic-type aftershock sequence model (HIST-ETAS model, in short) that forecasts the probability
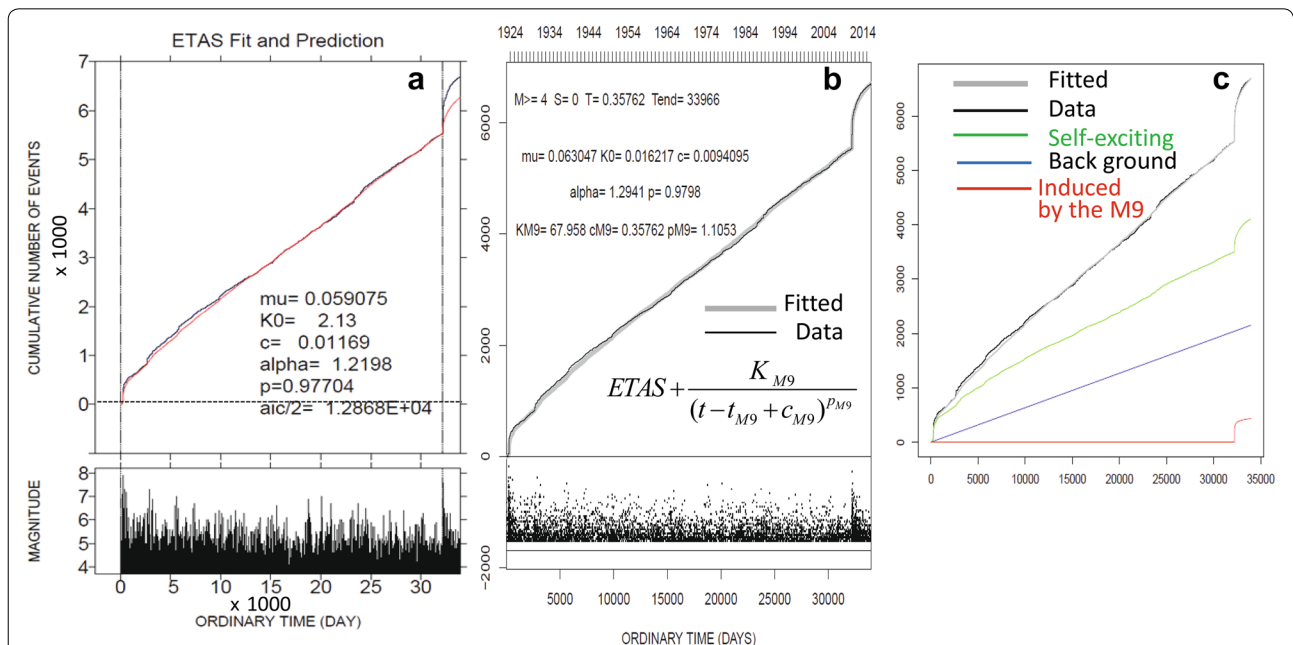

Fig. 2 Fitting of temporal models. The identical rising black lines in the three panels show the cumulative numbers of earthquakes of M4 and larger in the Kanto region, against the elapsed time over the entire period. **a** The red cumulative curve shows the theoretical numbers of M4 earthquakes and larger, from the beginning of the period. This was estimated using the ETAS model, fitted in the target period up until the time of the M9 Tohoku-Oki earthquake (indicated by the right side vertical dotted line), and extrapolated after that. **b** The thick gray line represents the expected cumulative curve obtained from model Eq. (1). **c** This panel shows the decomposition of the expected contributions to earthquake numbers, in the combined model Eq. (1), by background, self-triggering, and induced components

Ogata *et al. Earth, Planets and Space*   (2019) 71:113

Page 4 of 14

density of an earthquake occurrence at a future time instant t and at a location (x, y, z), under the history H_t of the above occurrence data, as follows:

$$
\begin{aligned}
\lambda_{\text{HIST-ETAS}}(t, x, y, z | H_t) = {} & \mu(x, y, z) \\
& + \sum_{\{j: t_j < t\}} \frac{K_0(\bar{x}_j, \bar{y}_j, \bar{z}_j)}{(t - t_j + c)^{p(\bar{x}_j, \bar{y}_j, \bar{z}_j)}} \frac{e^{\alpha(\bar{x}_j, \bar{y}_j, \bar{z}_j)(M_j - M_c)}}{e^{\alpha_0 {}^3/2 (M_j - M_c) {}^3/2}} \\
& \times \left[\frac{(x - \bar{x}_j, \ y - \bar{y}_j, z - \bar{z}_j) \, S_j^{-1} \begin{pmatrix} x - \bar{x}_j \\ y - \bar{y}_j \\ z - \bar{z}_j \end{pmatrix}}{e^{\alpha_0 (M_j - M_c)}} + d \right]^{-q},
\end{aligned}
\tag{2}
$$

where $(\bar{x}_j, \bar{y}_j, \bar{z}_j)$ and S_j are the centroid hypocenter and 3×3 variance–covariance matrix of a spatial cluster of aftershocks, respectively. These parameters are determined during the first 1 h, after automatically and objectively selected earthquakes, by analyzing all the detected aftershocks. Otherwise, they are the ordinary hypocenter coordinates and the 3×3 identity matrix, respectively. Additional file 1 provides more detail, but this procedure is simply a 3D hypocenter version from that used for 2D epicenters by Ogata (1998, 2004, 2011), Ogata et al. (2003), and Ogata and Zhuang (2016).

The background seismicity rate μ, self-triggering (aftershock) productivity K_0, α-value and p value are the set 3D location-dependent parameters. Furthermore, extending the temporal model in Eq. (1), we added an Omori–Utsu type function, for the decaying effect induced by the 2011 Tohoku-Oki M9 earthquake, in such a way that

$$
\begin{aligned}
\lambda(t, x, y, z | H_t) = {} & \lambda_{\text{HIST-ETAS}}(x, y, z | H_t) \\
& + \frac{K_{M9}(x, y, z) H(t - t_{M9})}{(t - t_{M9} + c_{M9})^{p_{M9}}},
\end{aligned}
\tag{3}
$$

where the productivity parameter K_{M9} of the Omori–Utsu type function is also set as 3D location dependent to show the intensity of the inducements in places where they occurred, following the Tohoku-Oki earthquake,

and t_{M9} denotes the M9 occurrence time at 14:46 18.1 on 11 March 2011 (JST).

Specifically, the location-dependent parameters take the following form:

$$
\begin{aligned}
\mu(x, y, z) &= \bar{\mu} \exp\{\phi_1(x, y, z)\}, \\
K_0(x, y, z) &= \bar{K}_0 \exp\{\phi_2(x, y, z)\}, \\
K_{M9}(x, y, z) &= \bar{K}_{M9} \exp\{\phi_3(x, y, z)\}, \\
\alpha(x, y, z) &= \bar{\alpha} \exp\{\phi_4(x, y, z)\}, \text{ and} \\
p(x, y, z) &= \bar{p} \exp\{\phi_5(x, y, z)\}
\end{aligned}
\tag{4}
$$

where $\bar{\mu}, \bar{K}_0, \bar{\alpha}, \bar{p}$ and $\bar{K}_{M9}$ are appropriately determined scalar parameters (see Table 1) and are called the reference parameters as explained below. Then, we constructed a 3D Delaunay tessellation (Tanemura et al. 1983) using the hypocenter coordinates, and some additional random points including on boundary surface of the cuboid. The above functions $\phi_1(x, y, z), \ldots, \phi_5(x, y, z)$ are then piecewise linear functions interpolated from the values at the vertices of the enclosing Delaunay tetrahedron, as described by Equations (S8) and (S15) in Additional file 1. We refer to such piecewise functions, $\phi_k(x, y, z); \ k = 1, \ldots, 5$, as the Delaunay functions. These are characterized by a number of coefficients (parameters) with more than five times the number of the earthquakes. Such a large number of parameters lead to an ill-posed problem, to be solved by maximizing the likelihood function. In response, we penalized the roughness (derivatives) of the ϕ-function to obtain a stable solution. Then, we considered the trade-off with the goodness of fit to the data (Good and Gaskins 1971). The optimal trade-offs for all location-dependent parameters are simultaneously attained by tuning five hyper-parameters (weights for the penalties) in a Bayesian framework using Akaike' Bayesian Criterion (ABIC, Akaike 1980) as was described for the 2D HIST-ETAS model in Ogata (2011); see S2 and

Table 1 Maximum likelihood estimates and reference parameters of the models

Param. unit	μ /day/deg^3	K_0 /day/deg^3	c day	α /mag.	p	d deg	q	K_{M9} /day/deg^3	c_{M9} day	p_{M9}
MLE	0.0164	4.16E−5	4.33E−3	1.29	0.98	2.9E−5	1.9	57.1	0.21	1.06
REF1	0.0662	2.97E−7	9.63E−3	1.29	0.98	5.8E−6	2.3	57.1	0.21	1.06
REF2	0.0634	9.62E−8	9.63E−3	1.29	0.98	5.8E−6	2.3	57.1	0.21	1.06
Weights	w_1	w_2		w_4	w_5			w_3		
	1.85	0.17		1000.	1000.			0.105		

Ogata *et al. Earth, Planets and Space* (2019) 71:113

Page 5 of 14

S4 in Additional file 1 for details. However, some preparatory procedures are required.

First of all, we assumed that all the characterizing parameters in Eq. (4) are constant, so that $\theta = (\mu, K_0, c, \alpha, p, \alpha_0, d, q, K_{M9}, c_{M9}, p_{M9})$ where $\alpha = \alpha_0$; and then applied Eq. (3), based on Eq. (2) the space–time ETAS (ST-ETAS) model, with externally induced effect. Next, we obtained the maximum likelihood estimates (MLEs; see Section S2.2 in Additional file 1) as listed in Table 1 (MLE).

These MLEs were then modified as the reference parameters within the location-dependent parameters $\mu(x, y, z) = \bar{\mu} \exp\{\phi_1(x,y,z)\}$, $K_0(x, y, z) = \bar{K}_0 \exp\{\phi_2(x,y,z)\}$, and $K_{M9}(x, y, z) = \bar{K}_{M9} \exp\{\phi_3(x,y,z)\}$; here $\bar{\mu}, \bar{K}_0, and \bar{K}_{M9}$ are modified from the MLEs using the zero sum mean calibration of $\phi_1(x,y,z)$, $\phi_2(x,y,z)$ and $\phi_3(x,y,z)$; whereas, the MLE scalar parameters $\hat{\alpha}_0, \hat{\alpha}, \hat{p}, \hat{c}, \hat{d}, \hat{c}_{M9}$, and $\hat{p}_{M9}$ remained the same in Eqs. (2) and (3). The resulting model, called the $\mu K_0 K_{M9}$-hierarchical space–time ETAS (HIST-ETAS) model, modified the constants $\bar{\mu}, \bar{K}$, $\bar{K}_{M9}$ and the other scalar baseline parameters, as given in Table 1 (REF1) as well as the optimal solutions of $\phi_1(x,y,z)$, $\phi_2(x,y,z)$ and $\phi_3(x,y,z)$ as explained in Section S2.3 of Additional file 1.

Finally, these MLEs were further modified for all of the reference parameters including the location-dependent parameters: $\alpha(x, y, z) = \bar{\alpha} \exp\{\phi_4(x,y,z)\}$, and $p(x, y, z) = \bar{p} \exp\{\phi_5(x,y,z)\}$, where $\bar{\mu}, \bar{K}_0, \bar{\alpha}, \bar{p}$, and $\bar{K}_{M9}$ were modified from the REF1 parameters by the zero sum mean calibration of each of $\phi_1(x,y,z)$, $\phi_2(x,y,z)$, $\phi_3(x,y,z)$, $\phi_4(x,y,z)$ and $\phi_5(x,y,z)$; whereas, the REF1 scalar parameters $\hat{\alpha}_0, \hat{c}, \hat{d}, \hat{c}_{M9}$, and $\hat{p}_{M9}$ remained the same in Eqs. (2) and (3). The resulting model, called the 5 parameters-hierarchical space–time ETAS (5pa-HIST-ETAS) model, modified the constants $\bar{\mu}, \bar{K}, \bar{K}_{M9}\bar{\alpha}, \bar{p}$, and the other scalar baseline parameters as given in Table 1 (REF2) as well as the optimal solutions of $\phi_1(x,y,z)$, $\phi_2(x,y,z)$ and $\phi_3(x,y,z)$ as explained in Section S2.4 of Additional file 1.

Using the fixed reference parameters in Table 1, we determined the Delaunay functions for the location-dependent parameters in Eqs. (2) and (3) (see Section S2.3 for the detail). In spite of the intensive computation required, the proposed models should be robust and should work reasonably well for future earthquake prediction in the 3D cuboid beneath the entire Kanto area. This expectation is found on the generation of optimal solutions for the parameters and subsequent forecasts at all vertices of the Delaunay tessellation; that is, the colored particles in Fig. 3. Linear interpolation, within the tetrahedron formed by the four nearest particles, then generates those statistics for any location within and beneath the Kanto region.

Some demonstrations of the 3D model

This section presents 3D images of the location-dependent parameters and occurrence rates on certain horizontal planes and plate surfaces that cross the 3D solution space. Specifically, Fig. 3 shows a horizontal plane, and the upper surfaces of the Pacific and Philippine Sea Plates beneath Kanto Plain. In the remainder of this paper, we provide 2D color images based on interpolation of the 3D solutions at the following surfaces: horizontal planes of depth 10 km and 20 km, and the upper surfaces of the Pacific and Philippine Sea Plates beneath Kanto Plain.

In the following, we evaluate the output of the estimation model, using the particular location-dependent parameters μ and K_{M9} in Eqs. (2) and (3), and describe notable characteristics of model solutions and their implications for earthquake forecasting beneath the Kanto region. The Supplementary Information details the solution of all the other parameters including self-triggering parameter K_0, which can be applied in generic short-term space–time large earthquake aftershock forecasting, as discussed in "Short-term, intermediate- and long-term 3D forecasting" section.

Short- and intermediate-term seismicity forecasts

The space–time model was estimated from data of $M \geq 4$ earthquakes in the period from the beginning of 1923 to the end of 2015. The earthquakes in the precursory first 2 years were used to adjust for the stationarity of the
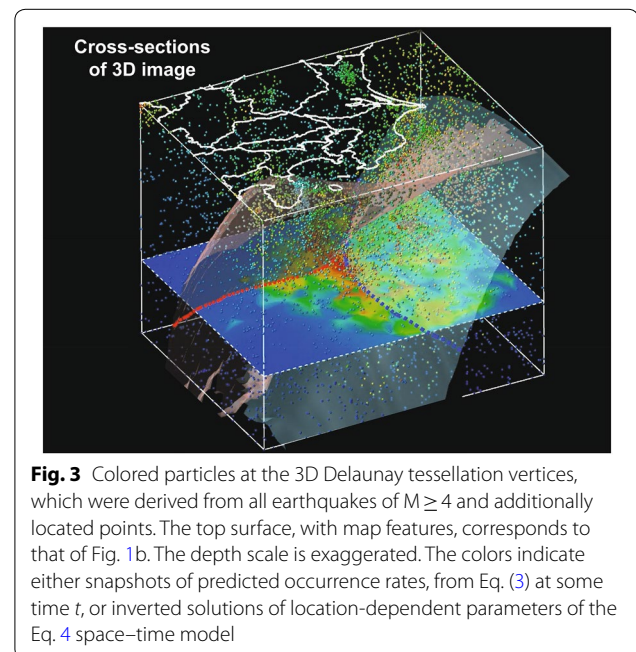

Fig. 3 Colored particles at the 3D Delaunay tessellation vertices, which were derived from all earthquakes of $M \geq 4$ and additionally located points. The top surface, with map features, corresponds to that of Fig. 1b. The depth scale is exaggerated. The colors indicate either snapshots of predicted occurrence rates, from Eq. (3) at some time *t*, or inverted solutions of location-dependent parameters of the Eq. 4 space–time model

Ogata *et al. Earth, Planets and Space*   (2019) 71:113

Page 6 of 14

(See figure on next page.)
Fig. 4 These colors show seismicity rate forecasts in the cuboid beneath the Kanto area at 16 June 2018. The units of color legend are event/day/deg^3, for a M $\geq$ 4 earthquake, where 'deg' means a degree of global latitude (i.e., 111.11 km). Plus signs are M $\geq$ 3.0 earthquakes that occurred after the forecast and until November 2018; those with depths from 0 to 15 km are shown on the 10-km plane (**a**), 16–30 km on the 20-km plane (**b**), and those with the depths of 5 km above to 10 km below the upper surface of each plate are shown on the plate forecast images (**c** and **d**). The contour interval of the rates is ln10, namely about 3 times as large

model, while the remaining data (target period) were used for parameter estimation.

Once the estimates were established, the model itself did not change, and prediction was based on additionally observed earthquakes by using the estimated space–time occurrence rates in Eqs. (3) with (2). For example, consider the forecasting, on June 16, 2018, of M $\geq$ 4 earthquake occurrence rates. Figure 4a–d shows 2D snapshots of the spatial occurrence rates on the surfaces described in Fig. 3.

To test this prospective prediction, we superimposed the locations of M $\geq$ 3.0 earthquakes (plus signs) that occurred near the depths of either of the two horizontal planes or of the upper plate surfaces, in the period till the end of November 2018. The M5.0 earthquake in panel (c) of Fig. 4 was the largest earthquake during the monitoring period. Assuming that the GR law holds in the range $3.0 \leq M \leq 5.0$, the panels suggest that the forecasts are working very well. Specifically, in the places where the forecast occurrence rate is high, moderate earthquakes are very likely in the short- and intermediate-term futures.

Background *μ*-rates useful for long-term forecasts
Figure 5 shows that the spatial pattern of the background event rates is relatively complex in comparison with other parameters such as *b*-value, *p* and *α* -values that are given in Figs. S1, S4, and S7, respectively, in Additional file 1. The rates are high in the mottled areas beneath the eastern offshore area and shallow crust, and on the plate boundaries. Furthermore, it is remarkably high for depths of 40–80 km in the clustered zone approximately 50 km northwest of Lake Kasumigaura (around 140.3E, 36.0 N), appearing to penetrate through the PHS to PAC Plates. This may be an effect of depth errors in the early period of the JMA catalog.

Similarly, the background rates are high beneath the central part of Kujukuri Beach (Chiba East Coast, around 140.4E, 35.5 N). We know that earthquake swarms, associated with slow slips on the PHS, occur here (Sagiya 2004; Hirose et al. 2014). However, directly below this region, there is another intensive earthquake cluster in the PAC. There are also swarms in shallow crust in the

western part of Kanto Plain, along a zone from north to south that includes the Mounts Fuji and Hakone.

The background rates are also high beneath northern Tokyo Bay on the upper interface of the PAC Plate. There have been a considerable number of historically disastrous earthquakes beneath the Tokyo Bay area (Utsu 1982, 2002). It is not known whether all these historical earthquakes, of long ago, are related to zones of high background occurrence.
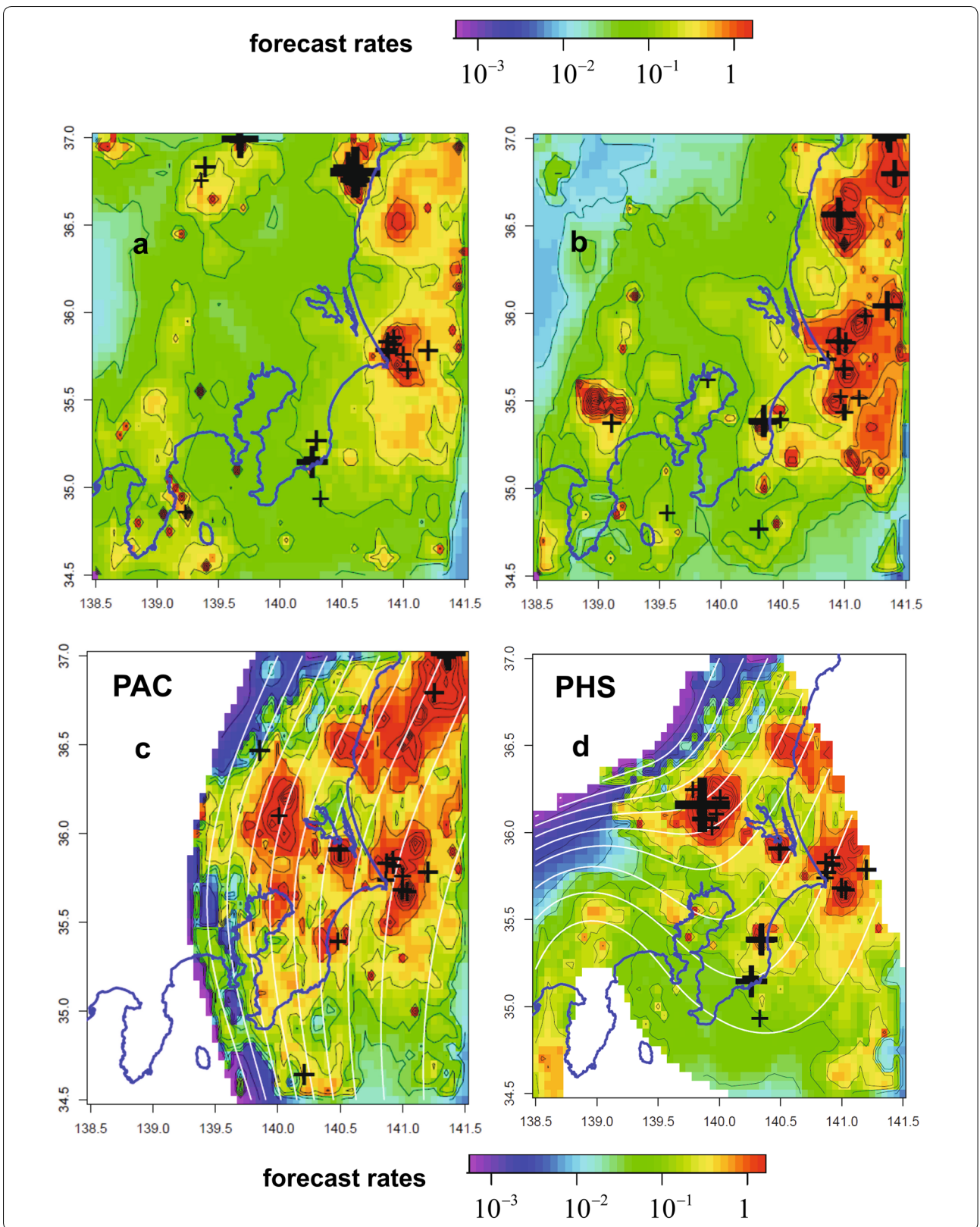
We can, however, confirm, according to the JMA catalog, that many large earthquakes of M6 and larger (black disks in Fig. 5), from the last 96 years, occurred at places where background rates are high. This mapping does not include the large aftershocks of the 1923 great Kanto earthquake of M7.9.
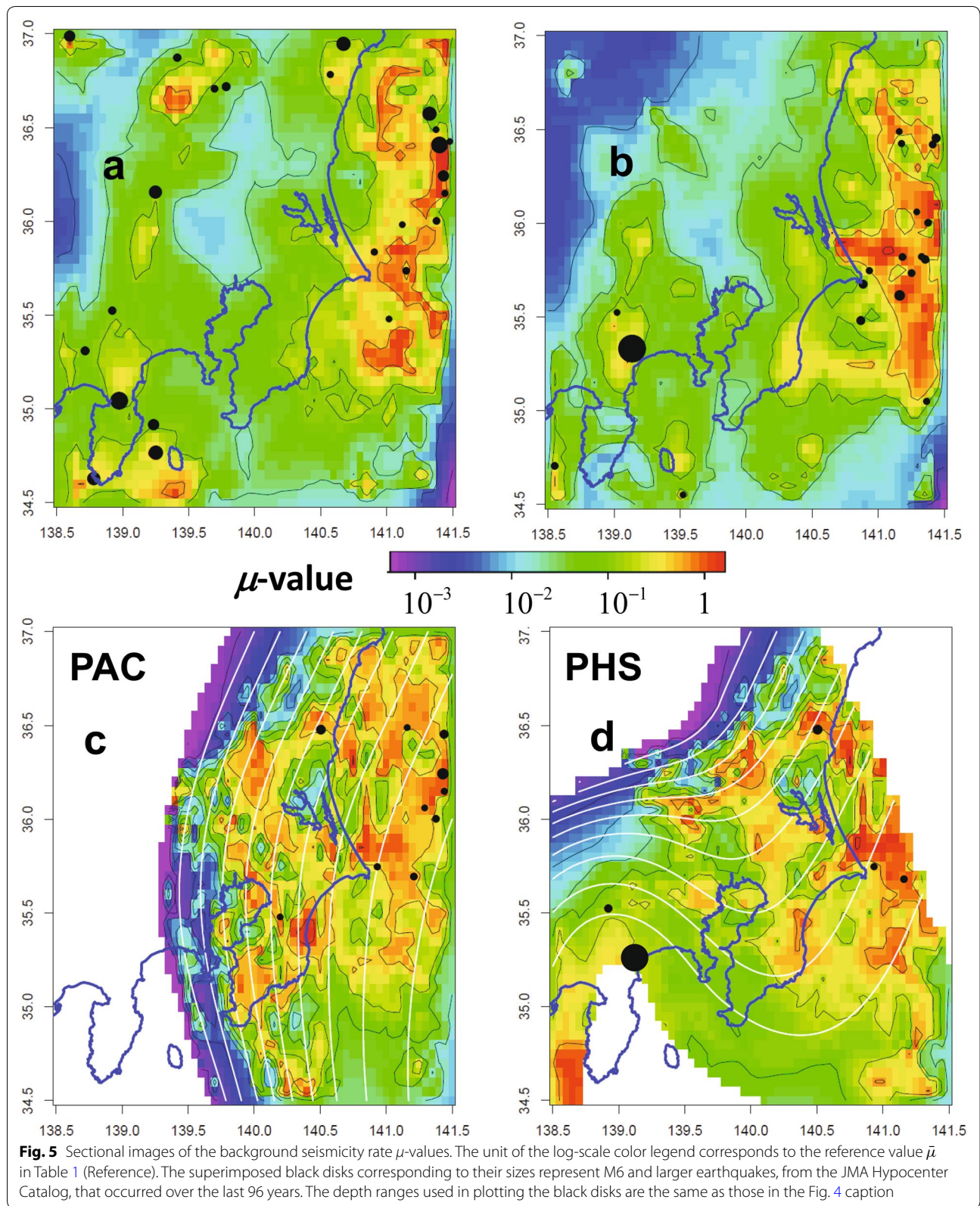
Our analysis suggests that variation in background rates of occurrence is important for long-term forecasting of large earthquakes.

Induced effect K_{M9} parameter
The K_{M9} images in Fig. 6 characterize the sizes of induced effects in the Kanto volume resulting from static stress changes after the 11 March 2011 M9 Tohoku-Oki earthquake. The zones of very high K_{M9} clearly include the great majority of the earthquakes that occurred in the month after the event (white circles in Fig. 6). The remarkable exceptions include shallow statically induced major earthquakes and their aftershocks (Fig. 6a); for example, at the northwestern edge (M6.7 Northern Niigata Prefecture), and also at Fujinomiya (Eastern Shizuoka Prefecture) of M6.4. Another inducement area is seen (Fig. 6d) in the zone near the upper surface of the PHS, 50 km NE from the Lake Kasumigaura. This seismicity enhancement cannot be explained solely by the static stress changes. More detailed studies are in Kumazawa and Ogata (Kumazawa 2013).

The inducing parameter K_{M9} appears to be intensively high in only some parts of the PAC Plate with high μ rates offshore in the east. On the other hand, the correlation with the background seismicity rate is less clear at about 40-km depth or deeper on both plates, and we see fewer triggering effects than in the eastern offshore area. There is a zone of high K_{M9} values on the PHS off the east coast
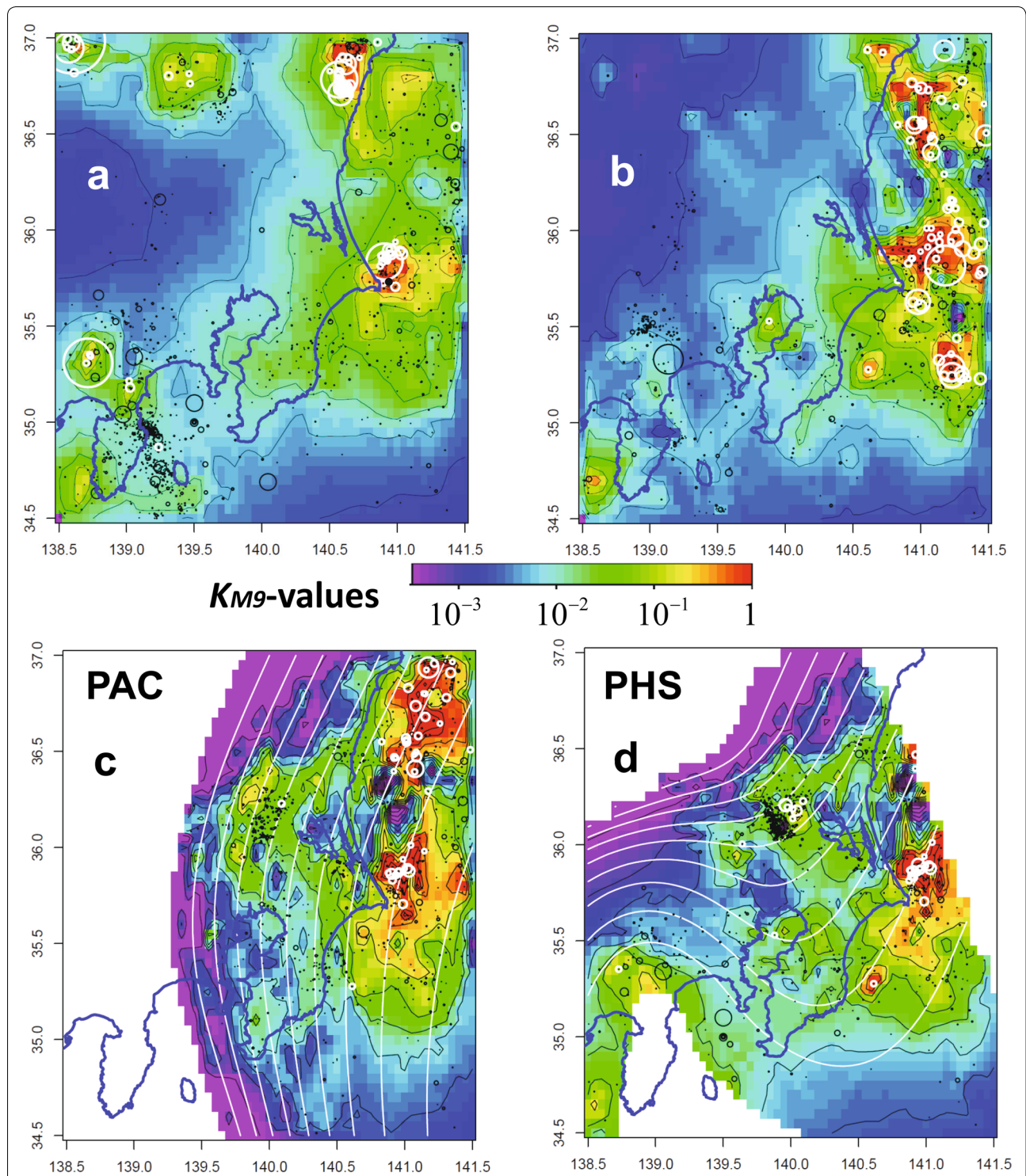
Ogata *et al. Earth, Planets and Space*   (2019) 71:113

Page 7 of 14

Ogata *et al. Earth, Planets and Space*   (2019) 71:113

Page 8 of 14

Fig. 5 Sectional images of the background seismicity rate μ-values. The unit of the log-scale color legend corresponds to the reference value $\bar{\mu}$ in Table 1 (Reference). The superimposed black disks corresponding to their sizes represent M6 and larger earthquakes, from the JMA Hypocenter Catalog, that occurred over the last 96 years. The depth ranges used in plotting the black disks are the same as those in the Fig. 4 caption

Fig. 6 Sectional images of K_{M9}-values. The units of the log-scale color legend correspond to the reference value $\bar{K}_{M9}$ in Table 1 (Reference). Small black circles and dots are the earthquakes of M4 and larger, that occurred near each plane and plate surface, throughout the entire period 1923–2015. White circles are the earthquakes of M4 and larger, that occurred within the month right after the M9 event. Both black and white markers increase in size with event magnitude: the white circles are five times larger than the black marks for events of the same magnitude. The depth ranges used in plotting the both disks circles are the same as those in the Fig. 4 caption

(See figure on next page.)

Fig. 7 Snapshots of occurrence rates of M ≥ 4 earthquake near the cross-sectional surfaces in the Kanto volume: plane at 10-km depth (**a–c**) and 20-km depth (**d–f**), and the upper surfaces of the Pacific Plate (**g–i**) and the Philippine Sea Plate (**j–l**). The columns show the dates of 2009.11.01, 2012.05.01 and 2018.06.30, respectively. The units of the color legend are event/day/deg^3 for M ≥ 4 earthquakes; and the black thin contour interval is 1.0 in the natural logarithmic scale; about three times as large as the linear scale

of the Boso Peninsula, which corresponds to the swarm zone associated with the triggered slow slip, 2 days after the M9 event (Hirose et al. 2014). On the whole, the inducing effect of K_{M9} is highest in the nearby part of the rupture source of the M9 Tohoku-Oki earthquake, on the upper PAC Plate boundary.

These K_{M9} images should be carefully compared with those showing the background seismicity rate μ in Fig. 5. As seen in Figure S9b in Additional file 1, the static stress changes decreased with the distance from the M9 slip source. The mottled pattern K_{M9} after de-trending such effect appears very similar to the mottled pattern of the background rate μ in each panel of Fig. 5; particularly, those on the plate boundaries of PAC and PHS in Fig. 5c, d. This means that, given a similar static stress rate, induced earthquakes are more likely to occur in zones of higher background rates.

Occurrence rate changes of earthquakes beneath the Kanto Plain before and after the 2011 Tohoku-Oki earthquake

Equation (3) estimates the occurrence rates of M ≥ 4 earthquakes at any time instant t. The three columns of Fig. 7 show the earthquake occurrence rates for 2009.11.01, 2012.05.01 and 2018.06.30, respectively. The four rows show the cross-sectional occurrence rates on the horizontal planes at 10-km and 20-km depths, and upper surfaces of PAC and the PHS Plates, respectively.

As the model-fitting period was from 1923 to 2015, the seismicity rates at 2009.11.01 and 2012.05.01 are interpolation. On the other hand, the occurrence rates at 2018.06.30 are extrapolations predicted using the same previous model for additional data from the period 2016–30 June 2018.

The first date 2009.11.01 precedes the 2011 Tohoku M9 earthquake, the second date 2012.05.01 is about 1 year after the M9, and the third 2018.06.30 is 7 years later. According to Fig. 7, the seismicity rate over the entire Kanto volume at 2009.11.01 is close to the estimated background rates as seen in Fig. 5. Occurrence rates increased significantly following the Tohoku-Oki earthquake, especially along the upper interface of the subducting Pacific Plate and in the north-east offshore.

Across the region, and especially in the crustal area and on and near the shallow plate boundaries (Figs. 7a–f), the occurrence rates increased substantially after the M9

Tohoku-Oki earthquake. In inland areas, in the following 7 years, rates then decayed back towards the pre-Tohoku seismicity level. However, in the eastern off coast areas, the rates have not yet reduced to pre-Tohoku levels.

The occurrence rates were particularly enhanced by the M9 Tohoku-Oki at shallower depths (30–40 km; Figs. 7, panel PAC a–c) on the upper PAC plate. The increase lasted for some time, and then reduced gradually but, comparing the contour numbers, not yet down to pre-M9 event levels (Fig. 7, panel PAC a). On the other hand, there was little change in seismicity rate on the upper PHS Plate boundary (Fig. 7, panels PHS, d–f) through the entire period, except for the zone offshore of Choshi City (Inubosaki), near the middle of the east coast, where the PHS Plate is almost riding on the PAC Plate. It is pertinent that slow slips beneath the Boso Peninsula were similarly active throughout the period (Hirose et al. 2014).

Discussions
Data quality
We note here that the quality of the JMA Hypocenter Catalog (JMA, 2018) is not perfectly homogeneous throughout the considered target period. Its accuracy before 1997 is not as good as after the unification of the catalog (see Acknowledgements).

Firstly, although the JMA has been updating event depths, to replace the pre-1997 grid search by free search, those from July 1976 to 1982 are still not updated and remain constrained to 10-km steps. Depth accuracy has been significantly improved since 1997; the standard errors of depth, after the unification, are now mostly less than 2 km.

Second, earthquakes in the eastern far offshore areas near the boundary of our studied region are biased towards deeper depths and dispersed, as seen in Fig. 1a, as a result of one-sided observation from land-based sensors.

In spite of this partial inhomogeneity in the JMA catalog, our fitted model, dependent on the accuracies of hypocenters, provides reasonable interpolation of 3D spatial occurrence rates including the spatial distribution of the aftershocks of the 1923 Kanto Earthquake. In particular, the interpolated 3D spatial occurrence rates for the period after 1997 are very accurate. Our model also the forecasts future 3D spatial seismicity rates, using processes justified by the present paper.
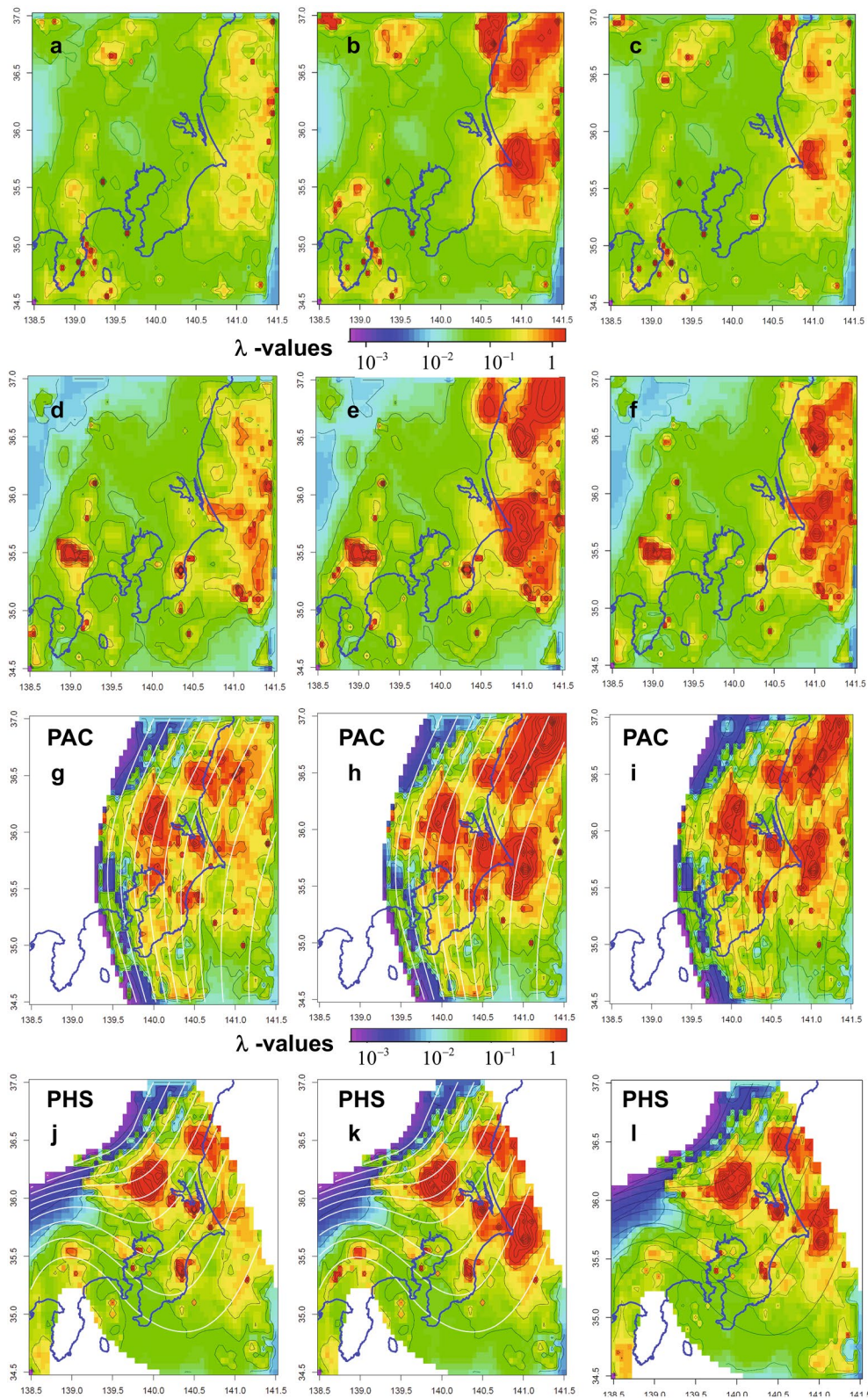
Relations to the Coulomb stress changes by the M9 Tohoku-Oki Earthquake

As an integrated approximation of the Tohoku-Oki slips, we used two rectangular source models reported by the Geospatial Information Authority of Japan (2011, Fig. 24 therein). At that time, due to the rake, dip and strike angles of the inter-plate earthquakes during the reverse faulting (see Fig. S9 in Additional file 1), the ΔCFS values on upper surface of the Pacific Plate and eastern parts of the PHS were positive (+1 to +10 bars); while locations closer to the M9 source had higher static stress changes. On the other hand, the western parts of the subducting PHS surface had smaller negative ΔCFS values (-0.8 ~ -0.2 bars) except for the offshore area east of Boso Peninsula where the strike and dip angles, due to the subducting plates, were similar to those of the PAC Plate (cf., plate boundary model in Fig. 1).

These findings are consistent with the changing seismicity rates in Fig. 7 (panels PAC and PHS), and with the corresponding K_{M9} images in Fig. 6c, d. Specifically, both the seismicity enhancements seen in the K_{M9} (x, y, z) images and the locations of earthquakes during the 1 month after the M9 event are consistent with the large ΔCFS values nearest to the slip source. This reminds us of why the seismicity changed significantly on the PAC Plate, whereas the seismicity on the PHS Plate remained almost unchanged, as described in "Induced effect K_{M9} parameter" section.

Short-term, intermediate- and long-term 3D forecasting

In the short term, after a large earthquake, we can forecast aftershocks using the 2D HIST-ETAS model as described in Ogata (2017). First, within an hour or so, only a quasi-real-time forecast using the isotropic matrix S_j in Eq. (2) is made. During that time, a cluster analysis for S_j is carried out; then, based on this, general non-isotropic space–time forecasting based on centroid hypocenters can be implemented (see Ogata 1998, 2004; Ogata et al. 2003; Ogata and Zhuang 2006; and Ogata 2011, for the 2D cases). As an example, we confirmed that retrospective forecasting, using the present model, of 3D space–time occurrence rates, 1 h after the 1923 Kanto earthquake of M7.9, reasonably well explained the JMA locations of the aftershock hypocenters.

Thus, in principle, the short-term probability forecast, in space–time–magnitude bins, can be calculated using the simple joint distribution of the separable combination between seismicity and magnitude:

$$\lambda(t, x, y, z; M \mid H_t) \, \mathrm{d}t \, \mathrm{d}x \, \mathrm{d}y \mathrm{d}z$$
$$= \lambda(t, x, y, z \mid H_t) \cdot \hat{\beta}(x, y, z) \, e^{-\hat{\beta}(x,y,z)(M-M_c)} \, \mathrm{d}t \mathrm{d}x \, \mathrm{d}y \mathrm{d}z,$$

(5)

where the estimation of the location-dependent parameter $\hat{\beta}(x, y, z) = \hat{b}(x, y, z) \ln 10$ for magnitude frequency is obtained similarly, as described in Section S1 of Additional file 1. Then, the spatial values of both the extended HIST-ETAS and b-value parameters at any location (x, y, z) can be interpolated by solving the relations in Additional file 1: Eq. (S7) and then interpolated using Additional file 1: Eq. (S8). In particular, the centroid hypocenter and variance–covariance matrix of a spatial cluster of aftershocks, represented by Eq. (2), can be determined using all detected and located earthquakes during the first one hour, say, after a large earthquake.

However, at each location, the location-dependent $\hat{b}(x, y, z)$ values determine the frequency distributions of small earthquakes near the threshold magnitude. Indeed, the magnitude distributions, in many local sub-volumes beneath Kanto plain, do not follow the GR law for larger magnitudes or take characteristic earthquake type shapes; alternative shapes, such as tapering, reflect the many modified Gutenberg–Richter magnitude frequency distributions (see Utsu 1999). Another issue is that the b-values for the main shocks and aftershocks can be significantly different (Utsu 1971). For example, Ogata et al. (2018) could not confirm that the magnitude forecasts, using location-dependent b-value throughout the Japan region, outperform the baseline GR law with $b = 0.9$ as a reference value. Hence, for now, it may be rather better to assume a generic magnitude frequency $\hat{\beta} = \hat{b} \ln 10$ with $\hat{b} = 0.9$, throughout the entire Kanto region, instead of $\hat{\beta}(x, y, z)$ in Eq. (4), to provide stable forecasting.

Furthermore, for real-time aftershock forecasting, the b-values should be estimated by taking the space–time incomplete earthquake detection rates into consideration right after a large earthquake (see Omi et al. 2013, Omi et al. 2014, 2015, 2016, 2018). To this end, we are investigating the extensions of the separable combination Eq. (4) to general cases (Ogata 2017; Ogata et al. 2018).

Intermediate- and long-term forecasts are considered as follows: suppose that the current time is S, and that we would like to forecast event probability over the period up to the time T. For an intermediate-term period [S, T], naive but time-consuming forecasts could be simulations based on the two models. Firstly, a sequence of magnitude {M_n, $n = 1, 2,...$} with $M_n \geq M_c$, using the standard or modified GR distributions with constant parameters, and with a single reference b-value (namely, $b = 0.9$) for the Kanto volume, is defined. Then (t_n, x_n, y_n, z_n), $M_n \geq M_c$, $n = 1, 2,..., N$, for the period [S, T] is simulated in the 3D volume V (Ogata 1981, 1998). This simulation procedure should be repeated many times to determine the variability of the potential seismicity under various scenarios. A similar procedure was applied in the Uniform California

Ogata *et al. Earth, Planets and Space*   (2019) 71:113

Page 13 of 14

Earthquake Rupture Forecast, Version 3 (UCERF3), referred to as UCERF3-ETAS (Field et al. 2017).

A more straight forward intermediate- and long-term forecasting approach assumes that the relationship

$$\int_S^T \lambda(t, x, y, z \mid H_S) \, dt$$
$$\approx \; (T - S) \cdot \frac{N(0, S)}{S} \frac{\mu(x, y, z)}{\iiint_V \mu(x, y, z) \, dx \, dy \, dz} \tag{6}$$

holds for any location. Then, the space–time forecast can be performed, by multiplying $\hat{\beta} \, e^{-\hat{\beta} \, (M - M_c)}$ with (5), for each location and magnitude range where the GR Law holds.

Conclusion

The temporal ETAS model shows how seismicity patterns in the Kanto region, before and after the M9 Tohoku-Oki earthquake, differ significantly. Hence, we modeled the seismic activity beneath the Kanto Plain using a combination of a 3D ETAS model and the Omori–Utsu formula for the induced effects of the M9 Tohoku-OKI earthquake. The model characteristic parameters are location dependent, and were estimated using piecewise linear functions on 3D Delaunay tessellation and an empirical Bayesian method using the ABIC. These parameterizations within our method provided high-resolution images in zones where hypocenters are dense. They accurately forecast, as we successfully demonstrated, the short-, intermediate- and long-term probabilities of occurrence beneath the Kanto plain.

Based on the hypocenter catalog for a century of earthquake events, we obtained inversion solutions for key location-dependent parameters, including the background seismicity rates, the self-exciting (aftershock) productivity rates, and the M9-induced productivity rate. The optimally inverted 3D spatial images of such characteristic parameters illustrate the discriminative seismicity patterns in the crust and on the subducting plates boundaries.

In particular, the background rate appears quite useful for long-term forecasting of large earthquakes. The external triggering factor shows the zones where the induced effect took place. These overlap with zones of high and intense background rate on the Pacific Plate boundary, but depend on distance from the M9 source. As yet, activity levels have not reduced back to those before the mega-event.

Supplementary information

Abbreviations
ABIC: Akaike's Bayesian Information Criterion; ΔCFS: Delta Coulomb Failure Stress; ETAS model: epidemic type aftershock sequence; HIST-ETAS model: hierarchical space–time ETAS model; GR Law: Gutenberg and Richter's Law; JMA: Japan Meteorological Agency; MLE: maximum likelihood estimate; PHS Plate: Philippine Sea Plate; PAC Plate: Pacific Plate.

Authors' contributions
YO led and designed the entire research at the request of NH. YO constructed the forecasting models, carried out the data analysis, interpreted the results, and drafted the manuscript. HT compiled the data for the analysis, KK drew all the figures. YO, HT, and NH discussed the results and commented on the manuscript. All authors read and approved the final manuscript.

Availability of data and materials
The JMA Hypocenter data used in this paper are available from the JMA (2018).

Competing interests
The authors declare that they have no competing interests.

Author details
[1] The Institute of Statistical Mathematics, 10-3 Midori-Cho,Tachikawa, Tokyo 190-8562, Japan. [2] Earthquake Research Institute, University of Tokyo, 1-1-1 Yayoi, Bunkyo-Ku, Tokyo 113-0032, Japan.

References
Akaike H (1980) Likelihood and Bayes procedure. In: Bernard JM, De Groot MH, Lindley DU, Smith AFM (eds) Bayesian statistics. Univ. Press, Valencia, pp 143–166. https://link.springer.com/chapter/10.1007/978-1-4612-1694-0_24 **(discussion 185–203)**
Dietrich J (1994) A constitutive law for rate of earthquake production and its application to earthquake clustering. J Geophys Res 99:2601–2618
Earthquake Research Committee (2004) Long-term evaluation for seismicity along the Sagami-Trough, p 31. https://www.jishin.go.jp/main/chousa/kaikou_pdf/sagami_2.pdf (in Japanese)

Ogata *et al. Earth, Planets and Space* (2019) 71:113

Page 14 of 14

Field EH, Milner KR, Hardebeck JL, Page MT, van der Elst Nicholas, Jordan TH, Michael Andrew J, Shaw BE, Werner MJ (2017) A spatiotemporal clustering model for the third uniform California earthquake rupture forecast (ucerf3-etas): toward an operational earthquake forecast. Bull Seismol Soc Am 107(3):1049–1081. https://doi.org/10.1785/0120160173

Geospatial Information Authority of Japan (2011), Crustal movements in the Tohoku District, (in Japanese with English captions), Report of the Coordinating Committee for Earthquake Prediction, 86: 184–272, http://cais.gsi.go.jp/YOCHIREN/report/kaihou86/03_34.pdf

Good IJ (1965) The Estimation of Probabilities. MIT Press, Cambridge, Massachusetts

Guo Y, Zhuang J, Hirata N (2018) Modeling and forecasting 3D-hypocenter seismicity in the Kanto region. Geophys J Int 214:520–530. https://doi.org/10.1093/gji/ggy154

Hashimoto C, Matsu'ura M (2006) 3-D simulation of tectonic loading at convergent plate boundary zones: internal stress fields in northeast Japan. Pure Appl Geophys 163(9):1803–1817. https://link.springer.com/article/10.1007/s00024-006-0098-y

Hashimoto C, Fukui K, Matsu'ura M (2004) 3-D Modelling of plate interfaces and numerical simulation of long-term crustal deformation in and around Japan. Pure Appl Geophys 161:2053–2067. https://link.springer.com/article/10.1007/s00024-004-2548-8

Hirose H, Matsuzawa T, Kimura T, Kimura H (2014) The Boso slow slip events in 2007 and 2011 as a driving process for the accompanying earthquake swarm. Geophys Res Lett 41:059791. https://doi.org/10.1002/2014gl059791

Ishibe T, Shimazaki K, Satake K, Tsuruoka H (2011) Change in seismicity beneath the Tokyo metropolitan area due to the 2011 off the Pacific coast of Tohoku Earthquake. Earth Planets Space 63(7):731–735

JMA (2018) The Seismological Bulletin of Japan, https://www.data.jma.go.jp/svd/eqev/data/bulletin/index_e.html

Kasahara, K, 1985. Patterns of crustal activity associated with the convergence of three plates in the Kanto–Tokai area, central Japan. Rep. Natl. Res. Cent. Disaster Prev. 35, 33–137. http://dil-opac.bosai.go.jp/publication/nrcdp/nrcdp_report/PDF/35/35kasahara.pdf

Kimura H, Kasahara K, Igarashi T, Hirata N (2006) Repeating earthquake activities associated with the Philippine Sea plate subduction in the Kanto district, central Japan: a new plate configuration revealed by interplate aseismic slips. Tectonophys 417(1):101–118. https://doi.org/10.1016/j.tecto.2005.06.013

Kumazawa T, Ogata Y (2013) Quantitative description of induced seismic activity before and after the 2011 Tohoku-Oki earthquake by nonstationary ETAS models. J Geophys Res 118(12):6165–6182. https://agupubs.onlinelibrary.wiley.com/doi/full/10.1002/2013JB010259

Ogata Y (1981) On Lewis' simulation method for point processes. IEEE Trans Inf Theory 27:23–31, https://pdfs.semanticscholar.org/9fb1/0a3c2dcec939784ce208e0e7e7fda4be895c.pdf

Ogata Y (1985) Statistical models for earthquake occurrences and residual analysis for point processes, *Research Memorandum* (Technical report) No. 288, https://www.ism.ac.jp/editsec/resmemo-j.html, and also in *Suri-Zisin Gaku* (*Mathematical Seismology*), Vol. 1, Ed. M. Saito, Cooperative Research Report, March 1986, The Institute of Statistical Mathematics, Tokyo. https://kyodo.ism.ac.jp/search/php/r_kyodo2.php?no=2

Ogata Y (1988) Statistical models for earthquake occurrences and residual analysis for point processes. J Am Stat Assoc 83:9–27. https://amstat.tandfonline.com/doi/abs/10.1080/01621459.1988.10478560#.Xawnzn9Us_U

Ogata Y (1989) Statistical model for standard seismicity and detection of anomalies by residual analysis. Tectonophysics 169:159–174. https://www.sciencedirect.com/science/article/pii/0040195189901911

Ogata Y (1998) Space-time point-process models for earthquake occurrences. Ann Inst Stat Math 50:379–402. https://www.ism.ac.jp/editsec/aism/pdf/050_2_0379.pdf

Ogata Y (2004) Space-time model for regional seismicity and detection of crustal stress changes. J Geophy Res 109(B3):B03308. https://doi.org/10.1029/2003JB002621

Ogata Y (2011) Significant improvements of the space-time ETAS model for forecasting of accurate baseline seismicity. Earth Planets Space 63(3):217–229. https://doi.org/10.5047/eps.2010.09.001

Ogata Y (2017) Forecasting of a large earthquake: an outlook of the research. Seismol Res Lett 88(4):1117–1126. https://doi.org/10.1785/0220170006

Ogata Y, Zhuang J (2006) Space-time ETAS models and an improved extension. Tectonophysics 413:13–23. http://bemlar.ism.ac.jp/zhuang/pubs/ogata2006tectno.pdf

Ogata Y, Katsura K, Tanemura M (2003) Modelling heterogeneous space-time occurrences of earthquakes and its residual analysis. Appl Stat (JRSSC) 52(4):499–509. https://www.jstor.org/stable/3592763?seq=1#page_scan_tab_contents

Ogata Y, Katsura K, Tsuruoka H, Hirata N (2018) Exploring magnitude forecasting of the next earthquake. Seismol Res Lett 89(4):1298–1304. https://doi.org/10.1785/0220180034

Omi T, Ogata Y, Hirata Y, Aihara K (2013) Forecasting large aftershocks within one day after the main shock. Sci Rep 3:2218. https://doi.org/10.1038/srep02218

Omi T, Ogata Y, Hirata Y, Aihara K (2014) Estimating the ETAS model from an early aftershock sequence. Geophys Res Lett 41:850–857. https://doi.org/10.1002/2013GL058958

Omi T, Ogata Y, Hirata Y, Aihara K (2015) Intermediate-term forecasting of aftershocks from an early aftershock sequence: bayesian and ensemble forecasting approaches. J Geophys Res Solid Earth 120(4):2561–2578. https://doi.org/10.1002/2014JB011456

Omi T, Ogata Y, Shiomi K, Enescu B, Sawazaki K, Aihara K (2016) Automatic aftershock forecasting: a test using real-time seismicity data in Japan. Bull Seismol Soc Am 106(6):2450–2458. https://doi.org/10.1785/0120160100

Omi T, Ogata Y, Shiomi K, Enescu B, Sawazaki K, Aihara K (2018) Implementation of a real-time system for automatic aftershock forecasting in Japan. Seismol Res Lett 90(1):242–250. https://doi.org/10.1785/0220180213

Parsons T, Console R, Falcone G, Murru M (2012) Comparison of characteristic and Gutenberg Richter models for time-dependent M ≥ 79 earthquake probability in the Nankai-Tokai subduction zone, Japan. Geophys J Int. https://doi.org/10.1111/j.1365-246x.2012.05595.x

Sagiya T (2004) Interplate coupling in the Kanto district, central Japan, and the Boso peninsula silent earthquake in May 1996. Pure Appl Geophys 161:2327–2342. https://link.springer.com/article/10.1007/s00024-004-2566-6

Tanemura M, Ogawa T, Ogita N (1983) A new algorithm for three-dimensional Voronoi tessellation. J Comput Phys 51:191–207. https://www.sciencedirect.com/science/article/pii/0021999183900876

Uchida N, Matsuzawa T, Nakajima J, Hasegawa A (2010) Subduction of a wedge-shaped Philippine Sea plate beneath Kanto, central Japan, estimated from converted waves and small repeating earthquakes. J Geophys Res 115:07309. https://doi.org/10.1029/2009jb006962

Utsu T (1971) Aftershock and earthquake statistic (III): analyses of the distribution of earthquakes in magnitude, time and space with special consideration to clustering characteristics of earthquake occurrence (1). J Fac Sci Hokkaido Univ 3:379–441. https://eprints.lib.hokudai.ac.jp/dspace/bitstream/2115/8688/1/3%285%29_p379-441.pdf

Utsu T (1982) Catalog of large earthquakes in the region of Japan from1885 through 1980. Bull Earthq Res Inst Univ Tokyo 57:401–463. https://repository.dl.itc.u-tokyo.ac.jp/?action=pages_view_main&active_action=repository_view_main_item_detail&item_id=32980&item_no=1&page_id=28&block_id=31

Utsu T (1999) Representation and analysis of the earthquake size distribution: a historical review and some new approaches. Pure Appl Geophys 155(2):509–535. https://link.springer.com/article/10.1007/s000240050276

Utsu T (2002) A list of deadly earthquakes in the World: 1500–2000. In: Lee WK, Kanamori H, Jennings PC, Kisslinger C (eds) International handbook of earthquake and engineering seismology, Part A. Academic Press, San Diego, pp 691–717. https://iisee.kenken.go.jp/utsu/index_eng.html

Utsu T, Ogata Y, Matsu'ura RS (1995) The centenary of the Omori formula for a decay law of aftershock activity. J Phys Earth 43(1–33):12. https://www.jstage.jst.go.jp/article/jpe1952/43/1/43_1_1/_article

Publisher's Note